

# A Plane Strain Model for Process-Induced Deformation of Laminated Composite Structures

ANDREW JOHNSTON\*, REZA VAZIRI\*\* AND ANOUSH POURSAARTIP

*Departments of Metals and Materials Engineering and Civil Engineering  
The University of British Columbia, Composites Group, Vancouver, B.C., V6T  
1Z4, Canada*

(Received July 14, 1999)  
(Revised June 14, 2000)

**ABSTRACT:** We present a plane strain finite element model for simulation of the development of process-induced deformation during autoclave processing of complex-shaped composite structures. A “cure-hardening, instantaneously linear elastic” constitutive model is employed to represent the mechanical behaviour of the composite matrix resin, and micromechanics models are used to determine composite ply mechanical properties and behaviour, including thermal expansion and cure-shrinkage. Structures with multiple composite and non-composite components can be simulated through the use of such strategies as adaptive time-stepping and incorporation of multiple composite plies into each finite element. The effect of process tooling can also be directly modelled through simulation of tool/part interfaces and post-processing tool removal. Integration of the residual deformation model with models for heat transfer and resin cure and resin flow permits analysis of all major identified sources of process-induced deformation during the autoclave process. Model application is demonstrated through prediction of process-induced deformation of a number of variations of a simple L-shaped laminate. The model is shown to provide accurate predictions of both spring-back angle and warped shape of the final part.

**KEY WORDS:** composites, modelling, processing, residual stress, spring-back, warpage, finite elements.

---

\*Now at National Research Council of Canada, Institute for Aerospace Research, Bldg. M-3 Montreal Road, Ottawa, Ontario, Canada, K1A 0R6.

\*\*Author to whom correspondence should be addressed at: Department of Civil Engineering, The University of British Columbia, 2324 Main Mall, Vancouver, B.C., Canada, V6T 1Z4, Tel. (604) 822-2800, Fax (604) 822-6901, e-mail: reza.vaziri@ubc.ca.

## INTRODUCTION

The combination of light weight, high stiffness and strength, and durability of advanced composite materials has made them an attractive option for numerous high-performance applications in aerospace and other industries. However, in order for composites to attain their full potential, their very high base costs must be offset by significant reductions in manufacturing costs relative to competing materials. One of the most promising paths to achieving required cost reductions is by exploiting the capability of autoclave processing to directly fabricate large, complex composite structures without resorting to extensive machining and fastening operations. However, current trial-and-error process development techniques are not well-suited to the complex task of developing the required robust manufacturing processes which can consistently produce high-quality structures within strict dimensional tolerance requirements.

A promising tool for both reducing process development costs and improving part quality is the application of numerical simulations of the autoclave process. As described in a recent review article [1], a number of increasingly complex and capable computational models for the autoclave process have been developed. Some of these models have focused on only one of the many phenomena involved in this process, such as heat transfer and resin reaction kinetics [2–4], resin flow [5,6], or stress development [7,8] while other models have been more broad in scope, examining a number of important processing phenomena and their interactions [9–12].

For the more comprehensive of these process models, a modular approach is typically employed for the overall model structure [9,12]. As illustrated in Figure 1, using this approach, the problem is divided into a series of “sub-models,” or “modules,” each responsible for performing a related set of tasks such as prediction of temperature and resin degree of cure (“thermochemical module”) or prediction of resin flow (“flow-compaction module”). Coupling between these modules is maintained by solving each in sequence as the solution marches forward in time. At the beginning of each time step, an “autoclave simulation” module, simulating automated autoclave control and response, updates all autoclave environmental variables including autoclave air temperature and pressure, and vacuum bag pressure. A more detailed description of the implementation of this type of approach is provided in Reference [12]. The current paper focuses on the formulation and numerical implementation of the module dealing with the development of residual strain and deformation during processing (the “stress-deformation module”).

Process-induced residual stress and deformation are two of the most critical issues in autoclave processing of composite structures. Residual stresses in themselves can have a significant impact on the performance of composite structures, potentially reducing both ultimate strength and fatigue life [13]. Process-induced

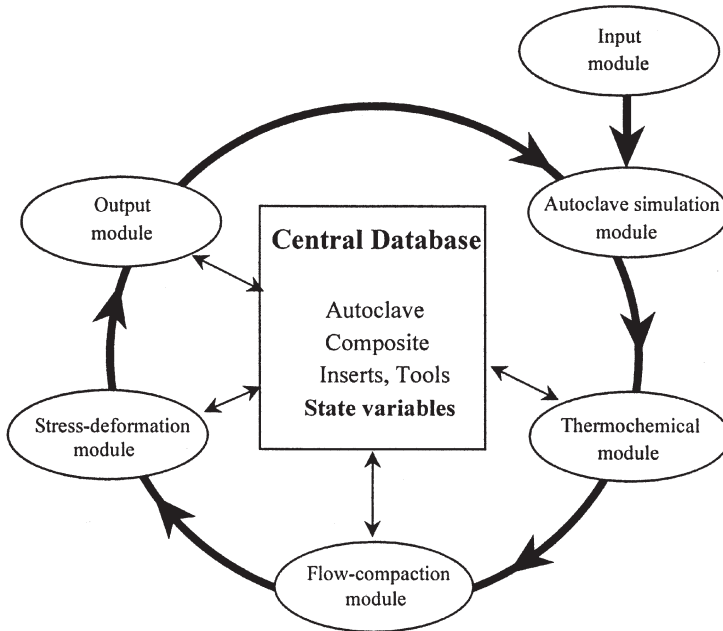


Figure 1. Schematic of COMPRO structure and program flow.

deformation has become an increasingly important issue as composite structures are employed in applications with strict tolerance requirements. Potential problems are especially acute for large, stiff structures where the loads required for force-fits are often prohibitive and a “shim-to-fit” strategy is not economical. While process-induced stress and deformation are to *some extent* unavoidable in autoclave processing, foreknowledge of the *amount* of each can be used to compensate in structure and tooling design. Thus, in many applications, the most important issue related to deformation is not necessarily reduction of its absolute value, but rather reduction of its variation.

As discussed in Adolf and Martin [14], the majority of previous analyses of process-induced residual stress and deformation in laminated composites have been based on the assumption that the only significant source of residual stress and deformation is “non-uniform” ply thermal strains, with ply thermal strains being generally much higher transverse to the fibres than along the fibre direction. However, more recent work has revealed a number of other important sources of residual stress and deformation including resin cure shrinkage strains [e.g., 8,11,14], non-uniform resin flow [15], cure gradients [11] and “tooling effects” [16,17]. For a stress and deformation model to consider *all* of these effects, it must examine the following phenomena throughout the entire process cycle:

- heat transfer within the structure and tooling and at their boundaries
- the kinetics of the matrix resin curing reaction and resin cure shrinkage
- flow of the resin within the curing composite and at its boundaries
- part and tooling thermal strains
- tooling mechanical constraints

Although two previous models examined stress development throughout processing [8,11] neither considered flow or tooling (mechanical) effects and both were limited to examination of relatively simple geometries (flat plates). Thus, despite the significant advances in the science of process modelling represented by recent models such as these, composites processors remained without an effective analytical tool for assisting in autoclave process development including tool and structural design.

To address this deficiency, a new special purpose finite element code called COMPRO [12,18,25] has been developed. By integrating a 2-D (plane strain) finite element stress and deformation analysis module with analyses of component temperature, resin degree of cure, resin flow and fibre bed compaction, this model can examine all major sources of process-induced stress and deformation identified in the literature in addition to the effects of tooling. Numerous techniques are employed to minimize the required computational effort including the use of an adaptive “time-stepping” algorithm, using an efficient “skyline” matrix solver, and allowing incorporation of multiple composite plies within each element. Coupled with continuing advances in available computing power, these methods allow examination of structures of significant size and complexity, including extensive sensitivity analyses, using very modest computational resources.

This paper outlines the development of the stress-deformation module in COMPRO and presents a representative case study demonstrating the application of this module to a simple processing problem.

## MODEL DEVELOPMENT

### Assumptions

As with all other modules of the COMPRO process model, the stress-deformation module examines a 2-D cross section of a component (Figure 2). This is believed to be adequate and appropriate for many composite structures, given that at least one dimension is usually very large compared to the other two. A similar assumption has also been used for prediction of process-induced stress in previous analyses [19,20].

The following major assumptions made in the present model should be noted:

- A plane strain condition is assumed to prevail in the  $x$ - $z$  plane and thus only a cross-section through the part is discretized.

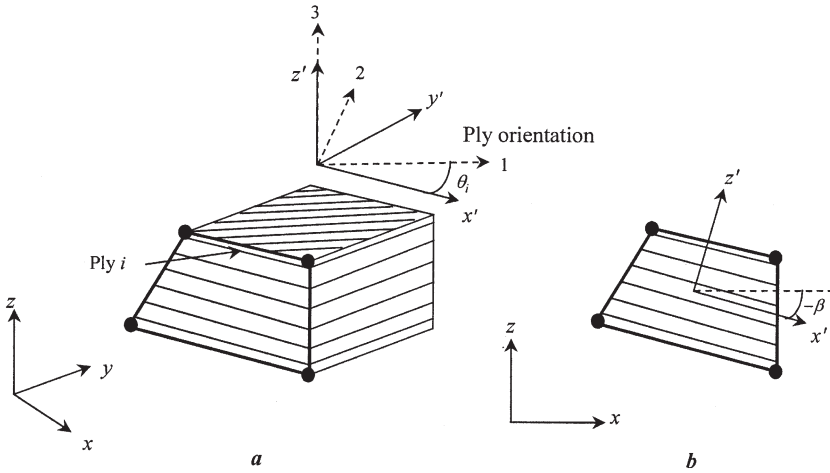


**Figure 2.** Composite element containing multiple plies, shown in: (a) isometric view and (b) plane view.

- All composite plies are assumed to run parallel to the  $\xi$ -axis of the element (see Figure 3) in which they are contained.
- All plies are assumed to be “unidirectional” (i.e. reinforced with continuous fibres, all aligned with one axis of the ply), with a fibre orientation in the “1” direction as illustrated in Figure 2. Woven plies currently must be modelled as a combination of unidirectional plies.
- The composite resin behaves as a “cure-hardening instantaneously linear elastic” (CHILE) material, with a modulus that increases monotonically with the degree of cure. Resin mechanical properties are assumed to be independent of moisture content.
- Fibre mechanical properties are a function of temperature only.
- All ply mechanical properties are orthotropic.
- Ply micromechanics models developed for fully cured composite plies exhibiting elastic behaviour are assumed to apply equally for plies which are not fully cured.
- The interface between a composite part and the process tooling can be represented by an elastic “shear layer” which remains intact until the tool is removed.
- Displacement boundary conditions remain constant throughout the solution until the simulation of “tool-removal.” During this calculation, a new set of displacement boundary conditions is applied as appropriate.
- The sole contributors to component nodal loads are thermal and cure shrinkage strains. External mechanical loads such as autoclave pressure are not considered in this paper<sup>1</sup>.

<sup>1</sup>The current version of the COMPRO code can handle nodal loads due to autoclave pressure.

## Governing Equations and Finite Element Discretization

The discretized form of the equilibrium equation for a body with built-in initial stresses and strains is:

$$\{\mathbf{F}\} = [\mathbf{K}]\{\delta\} \quad (1)$$

where  $\{\delta\}$  are the global nodal displacements, and the global load vector  $\{\mathbf{F}\}$  and stiffness matrix  $[\mathbf{K}]$  are given by (e.g. [21]):

$$\{\mathbf{F}\} = \sum_{e=1}^{nele} \left\{ \int_{\Omega_e} [\mathbf{B}]^T [\mathbf{C}] \{\epsilon_0\} d\Omega - \int_{\Omega_e} \{\mathbf{B}\}^T \{\sigma_0\} d\Omega + \int_{\Omega_e} [\mathbf{N}]^T \{\mathbf{F}_B\} d\Omega + \int_{\Gamma_e} [\mathbf{N}]^T \{\Phi\} d\Gamma \right\} \quad (2)$$

$$[\mathbf{K}] = \sum_{e=1}^{nele} \int_{\Omega_e} [\mathbf{B}]^T [\mathbf{C}] [\mathbf{B}] d\Omega \quad (3)$$

For the current plane strain problem, the various terms in the above equation are:

- $\{\epsilon\} = \{\epsilon_x \ \epsilon_z \ \gamma_{xz}\}^T$ , the strain field
- $[\mathbf{C}]$  = the plane strain material stiffness matrix
- $\{\epsilon_0\}, \{\sigma_0\}$  = initial strains and initial stresses
- $\{\mathbf{F}_B\} = \{F_x \ F_z\}^T$ , body forces
- $\{\Phi\} = \{\Phi_x \ \Phi_z\}^T$ , surface tractions
- $[\mathbf{N}]$  = matrix of element shape functions
- $[\mathbf{B}]$  = matrix of displacement shape function derivatives
- $nele$  = total number of elements in the discretized domain
- $\Omega, \Gamma$  = problem domain and traction boundary

To minimize storage requirements and solution time, Equation (1) is solved for nodal displacements,  $\{\delta\}$ , using a skyline solution algorithm.

In the current formulation, the domain is discretized using bilinear quadrilateral isoparametric elements [Figure 3(b)] which allows relatively easy meshing of laminates of arbitrary shape with a reasonable number of elements. To reduce the number of elements required to discretize a domain, it is permissible to incorporate multiple plies of any orientation within each composite material element as shown in Figure 2. Although it is not required that a whole number of plies be contained within an element (e.g., an element can contain 2.6 plies), the number of plies must be constant across the element “width” [i.e., the  $\xi$ -axis as shown in Figure 3(a)]. Ply stacking sequence for each composite material region is defined to begin from a “reference boundary” as illustrated in Figure 3(a). These reference boundaries are also used to define the orientation of the element local axes with respect to the global axes [angle  $-\beta$  in Figure 3(a) for all regions containing anisotropic materials.]

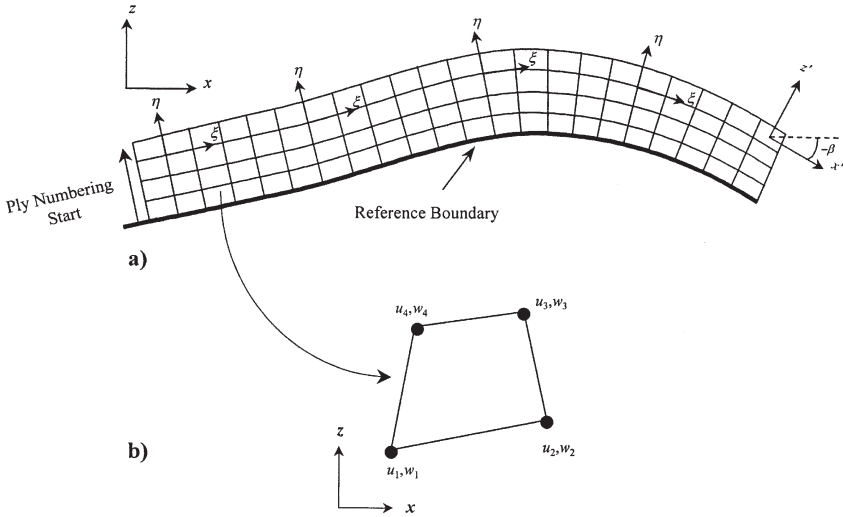


**Figure 3.** (a) Curved region, showing element local coordinates, local axes orientation and the region reference boundary and (b) bilinear quadrilateral element and degrees of freedom (i.e., displacements  $u_n$  and  $w_n$  in the  $x$  and  $z$  directions respectively, where  $n$  is the node number).

**Constitutive Relations**

*CALCULATION OF PLANE STRAIN MATERIAL STIFFNESS MATRIX*

For completeness, the development of the plane strain constitutive relations for a laminated medium comprised of orthotropic layers will be presented. In particular, the explicit form of the material stiffness matrix  $[C]$  for a single ply will be developed through appropriate transformations of the general 3-D matrix in the material principal directions. For all non-composite (i.e. homogeneous but orthotropic) materials, material principal directions are assumed to coincide with the element local axes ( $x'-z'$  in Figure 2). Composite material plies are assumed to be oriented at an angle  $\theta$  to the element  $x'-y'$  plane [Figure 2(a)].

Starting with the 3-D ply compliance relationship in the principal material axes, we can write

$$\{\varepsilon^*\} = [S^*]\{\sigma^*\} \tag{4}$$

where

$$\{\varepsilon^*\} = \{\varepsilon_1 \quad \varepsilon_2 \quad \gamma_{12} \quad \varepsilon_3 \quad \gamma_{13} \quad \gamma_{23}\}^T \tag{5}$$

and

$$\{\sigma^*\} = \{\sigma_1 \quad \sigma_2 \quad \tau_{12} \quad \sigma_3 \quad \tau_{13} \quad \tau_{23}\}^T \tag{6}$$

and  $[S^*]$  is a symmetric  $6 \times 6$  compliance matrix with terms calculated from the ply properties as:

$$[S^*] = \begin{bmatrix} \frac{1}{E_{11}} & \frac{-\nu_{12}}{E_{11}} & 0 & \frac{-\nu_{13}}{E_{11}} & 0 & 0 \\ & \frac{1}{E_{22}} & 0 & \frac{-\nu_{23}}{E_{22}} & 0 & 0 \\ & & \frac{1}{G_{12}} & 0 & 0 & 0 \\ & & & \frac{1}{E_{33}} & 0 & 0 \\ \text{Symmetric} & & & & \frac{1}{G_{13}} & 0 \\ & & & & & \frac{1}{G_{23}} \end{bmatrix} \quad (7)$$

This 3-D ply compliance matrix can be transformed to the element local axes using:

$$[S'] = [T_\theta]^{-1} [S^*] ([T_\theta]^T)^{-1} \quad (8)$$

where  $[T_\theta]$  is the standard 3-D stress/strain transformation matrix, defined here as:

$$[T_\theta] = \begin{bmatrix} \cos^2 \theta & \sin^2 \theta & \cos \theta \sin \theta & 0 & 0 & 0 \\ \sin^2 \theta & \cos^2 \theta & -\cos \theta \sin \theta & 0 & 0 & 0 \\ -2 \cos \theta \sin \theta & 2 \cos \theta \sin \theta & \cos^2 \theta - \sin^2 \theta & 0 & 0 & 0 \\ 0 & 0 & 0 & 1 & 0 & 0 \\ 0 & 0 & 0 & 0 & \cos \theta & -\sin \theta \\ 0 & 0 & 0 & 0 & \sin \theta & \cos \theta \end{bmatrix} \quad (9)$$

where  $\theta$  is the rotation of the ply local axes (1-2) with respect to the element local axes ( $x'-y'$ ) as defined in Figure 2 (counter-clockwise rotation is positive).

If we now impose the plane strain condition by suppressing all strain components normal to the plane being modelled (i.e.  $x-z$  or  $x'-z'$  plane), then it can be shown that the pertinent ply compliance matrix with reference to the local element axes,  $x'$  and  $z'$ , reduces to:

$$[\bar{\mathbf{S}}] = ([\mathbf{S}'_3] - [\mathbf{S}'_4][\mathbf{S}'_1]^{-1}[\mathbf{S}'_2]) \tag{10}$$

where

$$[\mathbf{S}'_1] = \begin{bmatrix} S'_{22} & S'_{23} & 0 \\ S'_{23} & S'_{33} & 0 \\ 0 & 0 & S'_{66} \end{bmatrix}; [\mathbf{S}'_2] = \begin{bmatrix} S'_{12} & S'_{24} & 0 \\ S'_{13} & S'_{34} & 0 \\ 0 & 0 & S'_{56} \end{bmatrix};$$

$$[\mathbf{S}'_3] = \begin{bmatrix} S'_{11} & S'_{14} & 0 \\ S'_{14} & S'_{44} & 0 \\ 0 & 0 & S'_{55} \end{bmatrix}; [\mathbf{S}'_4] = \begin{bmatrix} S'_{12} & S'_{13} & 0 \\ S'_{24} & S'_{34} & 0 \\ 0 & 0 & S'_{56} \end{bmatrix} \tag{11}$$

The *plane strain ply stiffness matrix* in the local element axes can then be calculated by inverting the compliance matrix, i.e.,

$$[\bar{\mathbf{C}}] = [\bar{\mathbf{S}}]^{-1} \tag{12}$$

Finally, the *ply stiffness matrix*  $[\mathbf{C}]$  in the global axes,  $x$ - $z$ , can be computed as follows:

$$[\mathbf{C}] = [\mathbf{T}_\beta]^T [\bar{\mathbf{C}}] [\mathbf{T}_\beta] \tag{13}$$

where  $[\mathbf{T}_\beta]$  is a transformation matrix defined as:

$$[\mathbf{T}_\beta] = \begin{bmatrix} \cos^2 \beta & \sin^2 \beta & \cos \beta \sin \beta \\ \sin^2 \beta & \cos^2 \beta & -\cos \beta \sin \beta \\ -2 \cos \beta \sin \beta & 2 \cos \beta \sin \beta & \cos^2 \beta - \sin^2 \beta \end{bmatrix} \tag{14}$$

with  $\beta$  being the rotation angle of the element local axes with respect to the global axes as defined in Figure 2(b).

**CALCULATION OF ELASTIC CONSTANTS**

All types of materials are assumed to be orthotropic and to exhibit an “instantaneously linear elastic” response. Thus, although the elastic constants may vary throughout the process simulation, the material behaviour at any given instant (i.e., during any time step) is assumed to be linear elastic.

All non-composite materials are assumed to exhibit orthotropic mechanical be-

haviour, with elastic constants that vary linearly with temperature only. Composite plies are assumed to be isotropic in the plane transverse to the fibre directions (i.e., transversely isotropic). Transversely isotropic fibre elastic constants are assumed to show a linear variation with temperature only. The isotropic matrix resin is modelled as a “cure-hardening instantaneously linear elastic” (CHILE) material. This designation indicates that the resin elastic modulus increases monotonically with the progression of cure.

Two models for prediction of the development of resin elastic modulus,  $E_r$ , with the cure process are currently used in the stress-deformation module, one adapted from Bogetti and Gillespie [11] and another developed as part of this work [25], with a formulation similar to the following:

$$\begin{aligned}
 E_r &= E_r^0 & T^* < T_{C1}^* \\
 E_r &= E_r^0 + \frac{T^* - T_{C1}^*}{(T_{C2}^* - T_{C1}^*)} (E_r^\infty - E_r^0) & T_{C1}^* < T^* < T_{C2}^* \\
 E_r &= E_r^\infty & T^* > T_{C2}^*
 \end{aligned} \tag{15}$$

where  $E_r^0$  is the “relaxed” resin modulus ( $E_r$  at  $T \gg T_g$ ),  $E_r^\infty$  is the “unrelaxed” modulus ( $E_r$  at  $T \ll T_g$ ) and  $T^*$  represents the difference between the resin temperature and the instantaneous resin glass transition temperature.  $T_{C1}^*$  and  $T_{C2}^*$  are constants, representing the critical values of  $T^*$  at the onset and completion of the glass transition [25]. For this model, a linear relation between glass transition temperature and degree of cure is assumed so that:

$$T^* = (T_g^0 + a_{Tg} \alpha) - T \tag{16}$$

where  $T_g^0$  is the uncured resin glass transition temperature,  $\alpha$  is the resin degree of cure, and  $a_{Tg}$  is a constant. As illustrated in Figure 4, this equation is essentially a more general form of a similar relation presented in Reference [11], with modulus dependence on temperature and the glass transition considered explicitly.

Given the calculated fibre and resin elastic constants and the fibre volume fraction  $V_f$  as inputs, transversely isotropic ply elastic constants can be determined from the ply micromechanics model developed by Bogetti and Gillespie [11] (see Appendix A).

### Solution Procedure

The solution technique used by the stress-deformation module can be described as an “incremental instantaneously linear elastic plane strain analysis.” Using this approach, the total solution at the end of a given time step is simply the summation

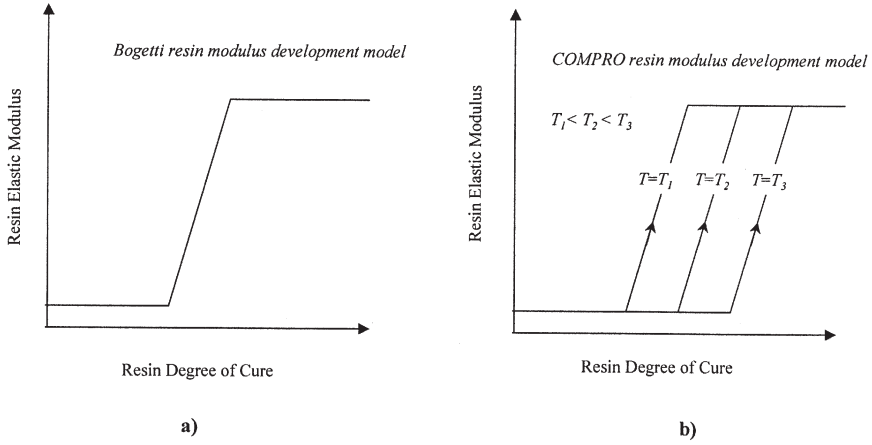


**Figure 4.** Models for resin elastic modulus development: (a) after Bogetti and Gillespie [11] and (b) COMPRO.

of the incremental elastic solutions from all previous steps. Thus, for example, the total nodal displacement at the end of module time step  $k$  is determined from the sum of calculated displacements at all previous steps, i.e.,

$$\{\delta\} = \sum_{i=1}^k \{\Delta\delta\}_i \tag{17}$$

The *change* in nodal displacements,  $\{\Delta\delta\}$ , during a time step is determined by solving the set of linear algebraic equations:

$$\{\Delta\delta\} = [\mathbf{K}]^{-1}\{\Delta\mathbf{F}\} \tag{18}$$

where  $\{\Delta\mathbf{F}\}$  is the *change* in the global force vector during the step and  $[\mathbf{K}]$  is the global stiffness matrix, calculated from Equation (3). The material elastic constants used to determine both  $\{\Delta\mathbf{F}\}$  and  $[\mathbf{K}]$  are calculated on an element-by-element basis at the beginning of each step from “averaged” element state variables (e.g., temperature, resin degree of cure, fibre  $V_f$ ) as illustrated in Figure 5. It should be noted that the matrix inversion indicated in Equation (18) is only symbolic as all matrix solutions in COMPRO are performed using a “sky-line” solution technique (e.g., [22]).

In the current analysis, external boundary loads on the structure have been ignored. Thus, the change in the element nodal force vector for each step,  $\{\Delta\mathbf{f}\}_e$ , is composed entirely of contributions from element thermal and cure shrinkage strains, i.e.,

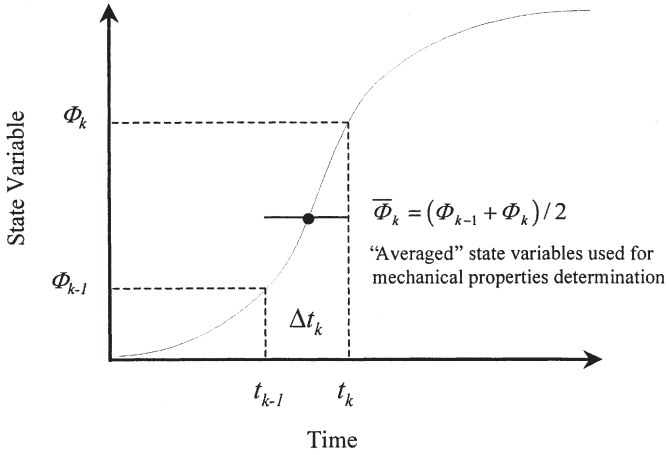


**Figure 5.** State variables used for calculation of mechanical properties used throughout time step  $k$ . These state variables are all available from previous calculations of the “up-stream” thermochemical and flow modules.

$$\{\Delta \mathbf{f}\}_e = \int_{\Omega_e} [\mathbf{B}]^T [\mathbf{C}] \{\Delta \boldsymbol{\varepsilon}_0\} d\Omega \tag{19}$$

where  $\{\Delta \boldsymbol{\varepsilon}_0\}$  is the change in the element “initial” strain vector, composed of thermal and cure shrinkage strains during the step (see Appendix A).

For elements containing non-composite materials or composite elements with only one ply (or a portion of one ply)  $\{\Delta \mathbf{f}\}_e$  and all other volume integrals are evaluated using a standard Gaussian integration technique employing four integration points per element [Figure 6(a)]. For elements containing multiple composite plies, a Gauss-Trapezoidal integration technique is used. As shown in Figure 6(b) a total of four integration points ( $2 \times 2$ ) are employed for each composite ply, two in the standard Gauss locations along the element  $\xi$  direction (i.e.  $\xi = \pm 1/\sqrt{3}$ ), and one at each ply interface in the  $\eta$  direction.

The numerical integration within each element can be expressed as:

$$\int_z \int_x f(x, z) dx dz = \int_{-1}^1 \sum_{k=1}^{nply} \left( \int_{-1}^1 f(\xi, \eta_k) |J|_k d\xi d\eta_k \right) = \sum_{k=1}^{nply} \sum_{l=1}^n \sum_{m=1}^n f(\xi_l, \eta_{km}) |J|_k w_l w_m \tag{20}$$

where  $n$  is the order of the integration ( $n = 2$  in this case) and  $w_l$  and  $w_m$  are the standard weight factors associated with the Gaussian and Trapezoidal integration

schemes. Also,  $nply$  is the number of plies,  $\eta_{km}$  is the matrix of integration points in the element  $\eta$  direction, and  $|\mathbf{J}|_k$  is the determinant of the  $ply$  (not the element) Jacobian matrix of transformation between the  $x$ - $z$  and  $\xi$ - $\eta$  planes.

After solving for the change in element nodal displacements,  $\{\Delta\delta\}_e$  in each step, the change in element *constraint* strains,  $\{\Delta\epsilon_\sigma\}_e$ , and element constraint loads,  $\{\Delta\mathbf{f}_\sigma\}_e$ , are determined as outlined in Appendix A. The element constraint strains are defined as the difference between the *total* element strains and the total combined element thermal and cure shrinkage strains. Element constraint loads are the difference between the *total* element nodal loads and the element nodal loads induced by thermal and cure shrinkage strains.

Throughout the model simulation, solution time step is dynamically adjusted to optimise the computational effort. Maximum time step size is calculated on the basis of the rate of solution change (e.g. temperature or degree of cure) and the rate of change in mechanical properties. Thus, calculations are performed more frequently when the model state variables are changing quickly (e.g. the part is curing rapidly) and less frequently during periods when they are changing slowly.

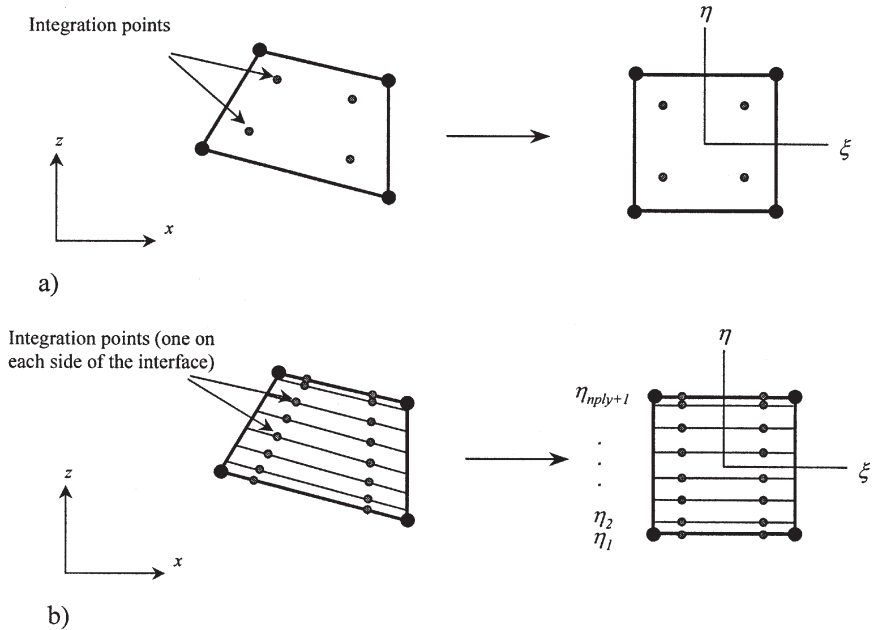


**Figure 6.** Integration points for calculation of element stiffness and load matrices: (a) for non-composite materials and elements containing only a single composite ply and (b) for elements containing multiple composite plies. Shown in both global (left) and element natural coordinates (right).

At the end of the simulated process cycle, the stress-deformation module performs two additional calculation steps to model processes which occur after the component is removed from the autoclave. The first of these is a simulation of part “cool-down.” This step simply involves resetting the component temperature uniformly to its initial value (usually room temperature), thereby removing any remaining elastic thermal strains. At the end of part cooling, the processed structure and any tooling typically remain attached with residual stresses remaining between them. To predict the “final” post-processed component shape, the process of separating the structure from the tooling is also simulated. This tool removal simulation is performed in a single (elastic) step and the change in the solution added to the pre-tool-removal solution. The procedure used for this simulation is illustrated schematically in Figure 7 and outlined below:

1. Create a finite element description of the tool removal problem. The new F.E. mesh is identical to that used in the cure cycle simulation, except that all “tooling” elements are removed and a new set of appropriate displacement boundary conditions is imposed.

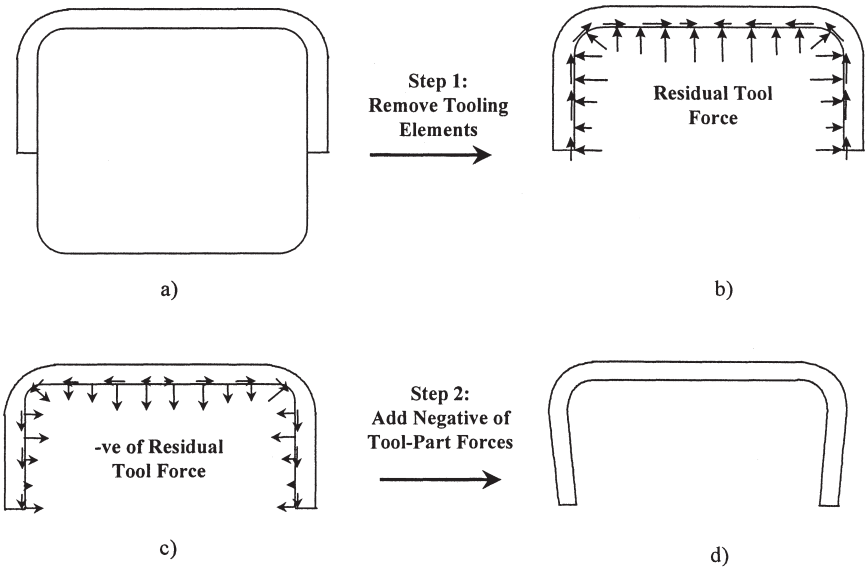


**Figure 7.** Schematic of the simulated tool removal process: (a) prior to tool removal, part and tool in equilibrium, part conformed to tool shape; (b) tooling removed, residual tool/part interface forces remain; (c) add negative of interface loads to obtain stress free interface and (d) predicted part shape after tool removal.

2. Assemble the tool removal global stiffness matrix,  $[\mathbf{K}_{\text{TR}}]$ , and initialize the tool removal global load vector,  $\{\mathbf{F}_{\text{TR}}\}$ , to zero.
3. Sum the *tooling element* nodal loads,  $\{\mathbf{f}_{\sigma}\}_e$ , for all nodes falling on the tool/part interface and add to the tool removal global load vector. The addition of these forces effectively creates a stress-free interface.
4. Solve for the part displacements during tool removal,  $\{\delta_{\text{TR}}\}=[\mathbf{K}_{\text{TR}}]^{-1}\{\mathbf{F}_{\text{TR}}\}$
5. Add the calculated displacements to the pre-tool-removal solution to find the final part shape.

The solution algorithm used by the stress-deformation module can be summarized as follows:

1. **Calculate** maximum allowable module time step, considering current rate of change of solution (i.e. maximum rate of change of modulus or strain within the domain).
2. **Check** if the *module* is to be RUN; if not, **RETURN** to MAIN program.
3. **Update** mechanical properties (elastic constants, thermal expansion coefficients, etc.).
4. **Reset** global stiffness matrix  $[\mathbf{K}]$  and global nodal force vector  $\{\mathbf{F}\}$ .
5. **Loop** over all model elements.
6. **Calculate** element stiffness matrix  $[\mathbf{k}]_e$  and change in nodal load vector,  $\{\Delta\mathbf{f}\}_e$  using Equations (3) and (19), respectively.
7. **Calculate** change in element initial strain vector,  $\{\Delta\epsilon_0\}_e$  (see Appendix A).
8. **Apply** essential boundary constraints (i.e., fixed and sliding nodes).
9. **Assemble**  $[\mathbf{k}]_e$  and  $\{\Delta\mathbf{f}\}_e$  into global matrices  $[\mathbf{K}]$  and  $\{\mathbf{F}\}$ .
10. **Solve** for change in nodal displacements,  $\{\Delta\delta\}=[\mathbf{K}]^{-1}\{\Delta\mathbf{F}\}$ .
11. **Calculate** the change in element *constraint* strains,  $\{\Delta\epsilon_{\sigma}\}_e$  (see Appendix A).
12. **Calculate** the change in element *constraint* loads  $\{\Delta\mathbf{f}_{\sigma}\}_e$  (see Appendix A).
13. **Calculate** total nodal displacement by summing over all time steps, using Equation (17).
14. **RETURN** to MAIN program

## Model Verification

Before applying the model to predict the development of residual stress and deformation in real components, a number of verification runs were performed to verify the element formulation and implementation. These runs were used to compare the model predictions with exact solutions and results of other established numerical codes for a number of simple geometries and material types.

One of the most important and illustrative verification tests employed was the calculation of “spring-back” of a curved composite laminate as a result of a uniform temperature change. Spring-back of curved composite shapes due to non-uniform thermal strain (i.e. difference in strain in  $x$  and  $z$ ) is one of the most

important and widely recognised sources of process-induced deformation in composite materials [16].

The part geometry and nodal constraint conditions employed throughout the verification run are illustrated in Figure 8(a) along with the finite element mesh for the “nominal” case. In all cases, the part inner surface is used as the region “reference boundary” from which ply layup and material principal directions are defined. The elastic constants and thermal strain coefficients used are for a “typical” cured carbon fibre epoxy material and are tabulated in Table 1. In all cases, a total temperature difference of 180°C is applied.

For a symmetric laminate, spring-back due to a temperature change can usually be estimated very closely using the following equation [16]:

$$\Delta\theta = \theta_i \left[ \frac{(\alpha_\theta^T - \alpha_R^T)\Delta T}{1 + \alpha_R^T\Delta T} \right] \quad (21)$$

where  $\theta_i$  is the “included” angle (90° in this case), and  $\alpha_R^T$  and  $\alpha_\theta^T$  are the thermal strain coefficients in the radial and circumferential directions, respectively. Note that the convention used here is that positive spring-back corresponds to a *decrease* in the included angle [see Figure 8(b)].

Model predictions for four different types of laminate layup and a variety of mesh densities are shown in Table 2 and compared to predictions of the commercial finite element code MSC/NASTRAN®. As expected from theory, the  $[90]_n$  (i.e. with fibres perpendicular to the plane shown in Figure 8) laminates exhibit no spring-back whatsoever due to the assumed isotropy in the plane of interest. The greater predicted spring-back of the  $[0]_n$  laminates as compared to the quasi-isotropic laminates ( $[0/45/90/-45]_S$  and  $[0/45/90/-45/-45/90/45/0]_S$ ) is initially surprising since the difference between circumferential and radial thermal strains is normally greater for the latter layup [23,24]. The opposite is found in this case due to the use of a plane strain formulation which suppresses both the large out-of-plane thermal strains of the  $[0]_n$  laminates and the much smaller strains of the quasi-isotropic laminates in this direction.

As shown in Table 2, the predictions of the current model compare very well

**Table 1. Mechanical properties used in the thermal strain spring-back verification test.**

Parameter	Value(s) Employed
Elastic constants (stiffnesses in GPa)	$E_{11} = 122.2, E_{22} = 9.88, E_{33} = 9.88, G_{12} = 5.18,$ $G_{13} = 5.18, G_{23} = 3.36, \nu_{12} = 0.268, \nu_{13} = 0.268, \nu_{23} = 0.471$
Thermal expansion coefficients ( $\times 10^{-6}/^\circ\text{C}$ )	$\alpha_1^T = 0.60, \alpha_2^T = 28.6, \alpha_3^T = 28.6$

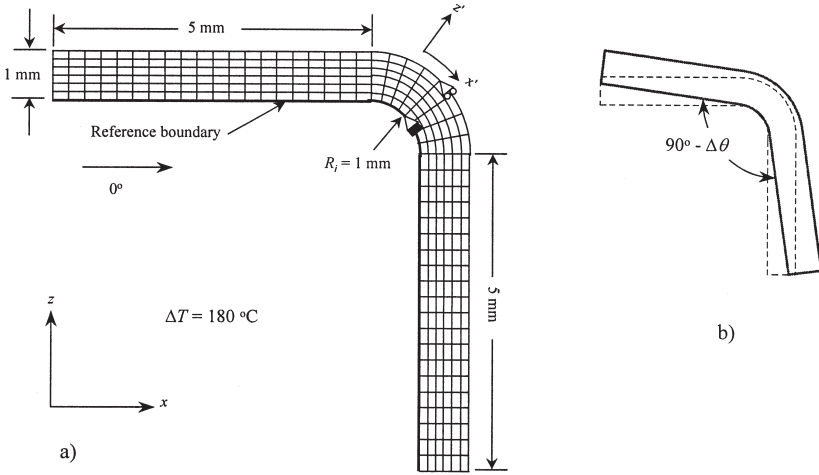


**Figure 8.** (a) Geometry employed for the thermal strain spring-back verification test (note that the finite element mesh shown is for the nominal case only and (b) change in laminate shape following temperature change, showing springback angle  $\Delta\theta$ ).

with those of NASTRAN in all cases. These results also show that the model predictions are *not* highly sensitive to the number of plies per element, verifying that both the standard Gaussian integration technique (used when the number of plies per element is 1) and the Gauss-Trapezoidal technique (used when number of plies per element > 1) give essentially identical results.

**Table 2. Model spring-back predictions for various cured carbon fibre/epoxy laminates subjected to a temperature change of  $\Delta T = 180^\circ\text{C}$ .**

Laminate Layup	Number of Plies per Element	Model Prediction	NASTRAN Prediction (1 ply per Element)	Difference (%)
[0]	0.167	-0.6612°	—	—
[0] <sub>10</sub>	1.67	-0.6614°	-0.6611°	-0.05
[90]	0.167	0.0000°	—	—
[90] <sub>10</sub>	1.67	0.0000°	—	—
[0/90/0/90] <sub>s</sub>	1.0	-0.6126°	-0.6126°	0.00
[0/90/0/90] <sub>2s</sub>	2.0	-0.6121°	—	—
[0/45/90/-45] <sub>s</sub>	0.5	-0.5934°	—	—
[0/45/90/-45] <sub>s</sub>	1.00	-0.5939°	0.5931°	-0.13
[0/45/90/-45] <sub>s</sub>	2.00	-0.5936°	—	—
[0/45/90/-45/-45/90/45/0] <sub>s</sub>	4.00	-0.5941°	—	—

**MODEL APPLICATION**

In this section, the model is used to predict process-induced deformation of various L-shaped, angle laminates (channel sections) with the geometry shown in Figure 9(a), and these predictions are compared to experimental measurements.

**Experimental Procedure**

In the experimental component of this work, four different types of 24-ply L-shaped laminated specimens were laid up ply-by-ply on a solid convex aluminum tool as illustrated in Figure 9(b). Three of the laminates employed symmetric layups, one quasi-isotropic ( $[90/-45/+45/0]_6$ ), and two unidirectional ( $[0]_{24}$ ,  $[90]_{24}$ ). Three specimens with each of these layups were processed in an autoclave using variations of the nominal process cycle shown in Figure 9(c). A single speci-

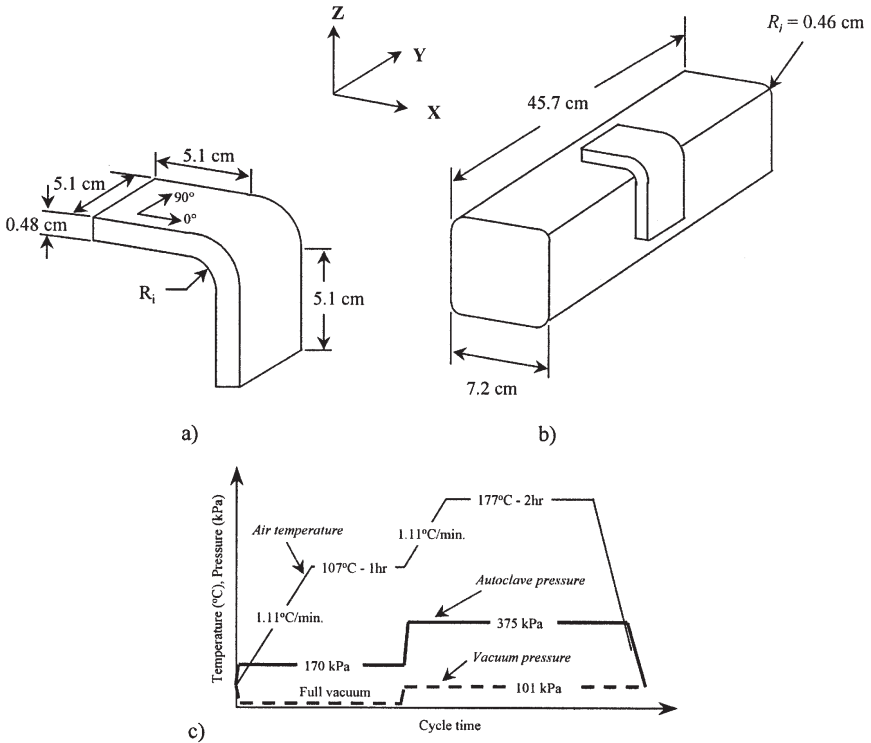


**Figure 9.** (a) Angle laminate geometry, (b) laminate mounted on solid convex aluminum tool and (c) nominal autoclave process cycle.

men of an unsymmetric  $[90_{12}/0_{12}]$  layup was also fabricated so that model predictions for severely warped components could also be examined. The properties used in each case were those for unidirectional Hercules AS4/8552, a second generation carbon fibre/epoxy prepreg [25].

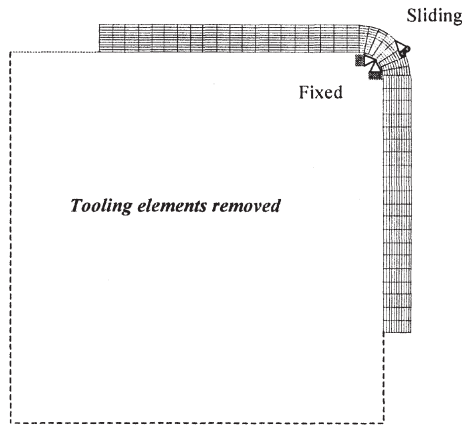
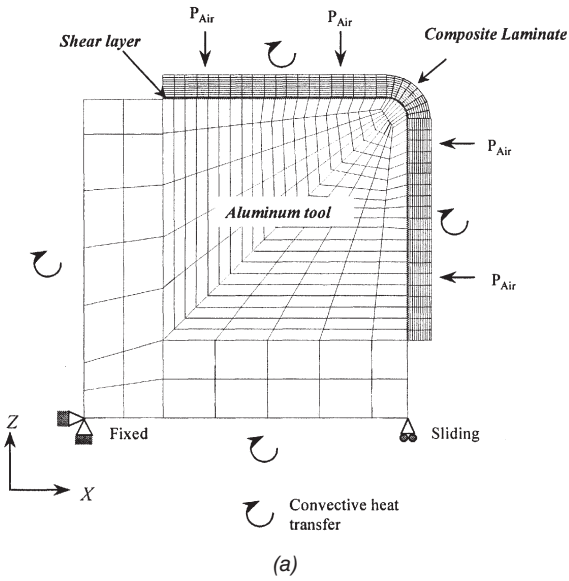
After processing, the laminates were debagged, removed from the aluminum tool and their edges trimmed. A digital image was then taken of the edge of the specimen tool-side surface and digital analysis software used to determine the total “included angle,”  $\theta_i$ , from points on the extreme ends of each trimmed “arm.” The spring-back angle,  $\Delta\theta$ , was then calculated by subtracting the measured angle from the original 90 degrees (positive spring-back indicating a reduction in included angle). Three spring-back measurements were taken for each specimen and the average value recorded. Measurement repeatability indicates an accuracy of about  $\pm 0.2^\circ$  for this technique.

### Numerical Simulation

The finite element representation used for the angle laminate analysis is shown in Figure 10. A fairly coarse mesh with a total of 762 isoparametric quadrilateral elements was employed in this case with 480 elements in the part and the remainder in the tool and tool/part shear layer. Previous simulations, including the model verification tests shown above, indicated that this would provide an adequate mesh density for this problem. Sensitivity analyses demonstrated that the employed automatic time stepping parameters chosen (which allowed the model to dynamically choose a time step from 1 s to 30 s in this case) were appropriate for a converged solution to be reached.

The boundary conditions employed for this case are as follows:

- **Heat transfer:** A convective heat transfer boundary condition was applied on all external boundaries. A uniform heat transfer coefficient was assumed and was calculated in this case to match measured part and tool temperatures during processing.
- **Resin flow:** The inner surface of the part was fixed to the tool and autoclave air pressure was applied to the top surface of the part. All boundaries were made impermeable to resin flow in order to simulate a “no-flow” condition (see Hubert et al. [6]).
- **Mechanical:** During processing, single points on the tool were set to “fixed” and “sliding” as shown in Figure 10(a). A thin elastic “shear layer” (0.37 mm in thickness), with a modulus set equal to that of the aluminum tool, was placed between the tool and the part, simulating perfect tool/part bonding. During the tool removal process, all nodes but one along the part “line of symmetry” were set to “sliding”; this single node was set to “fixed” to prevent rigid-body motion [see Figure 10(b)].



Scale:  
2.5 cm

(b)

**Figure 10.** Finite element representation of angle laminate: (a) during processing and (b) simulation of tool removal process.

### MATERIAL PROPERTIES

The thermophysical and mechanical properties employed in this simulation for both the aluminum tool and the carbon fibre/epoxy material, including characterisation tests employed, are described in detail in Reference [25]. Material properties used in simulation of resin flow and fibre bed compaction are provided in Reference [6].

After the completion of the simulated process cycle, a simulation of the tool removal process was performed and the spring-back angle for the various modelled laminates was determined using a numerical technique analogous to that used for the real part. Total solution time in all simulated cases was less than 20 minutes on a PC employing an Intel Pentium Pro™ 200 MHz processor.

### Comparison of Experimental and Numerical Results

As shown in Figure 11 and Table 3, the predicted relative magnitude of the spring-back angle as a function of layup for the symmetric laminates was found to correspond with the experimental measurements. Numerical predictions also compare quite well with experimental measurements for both the quasi-isotropic laminates  $([90/+45/-45/0]_6)$  and the  $[0]_{24}$  laminates. However, for the  $[90]_{24}$  laminates, predicted spring-back angle was much lower than measured. Before examining this further, it is instructive to compare these results with those obtained by other researchers. In similar measurements of spring-back in L-shaped carbon fibre/epoxy laminates, both Rennick and Radford [26] and Patterson et al. [27] observed the same trend in spring-back angle with part layup as seen here, i.e.,  $\Delta\theta_{[90]_n} \ll \Delta\theta_{[0]_n} < \Delta\theta_{[90/+45/-45/0]_n}$ . As discussed, this trend can be explained by the relative difference in radial and circumferential thermal and cure shrinkage strains for the different laminates.

This difference in strains, however, cannot entirely explain the observed specimen behaviour on its own. One problem is that the spring-back angles predicted for this phenomenon on its own are too small (see Figure 11). While the predicted *differences* between the spring-back angles for the different laminates are roughly the same as observed here (and by previous researchers [26,27]), the predicted magnitude is about  $1^0$  too small in all cases. Clearly, contrary to traditional assumptions, there are important sources of residual deformation in this case other than those arising from anisotropies in the coefficient of thermal expansion (CTE) and coefficient of cure shrinkage (CCS).

Close examination of the predicted final laminate shape reveals that, while non-uniform thermal and cure shrinkage strains (due to CTE and CCS anisotropies) would result in changes in corner geometry only, the current model predicts that the laminate “arms” will also warp slightly. Measurements of spring-back angle at various locations along the arm of the simulated  $[90/+45/-45/0]_6$  laminate show that the spring-back immediately adjacent to the corner is only approximately

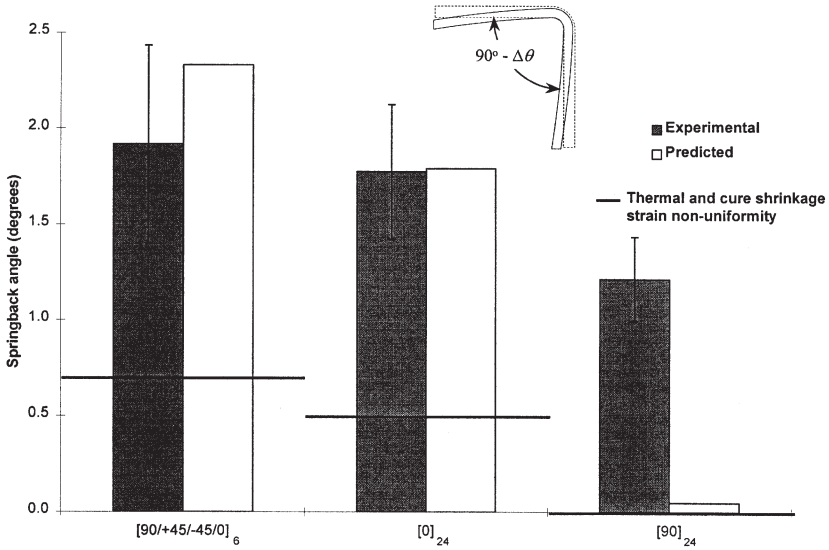


**Figure 11.** Comparison of experimental and predicted spring-back angles for angle laminates. Error bars on experimental values represent  $\pm 1\sigma$  variation from the mean. Also shown is the predicted spring-back from strain non-uniformity alone.

1.06°. The difference between this value and the measured value of 2.33° at the end of the arm is due to arm warpage. Although this might seem to constitute a very large amount of warpage, as shown in Figure 12, the predicted maximum deviation of the arm edge from a straight line is only about 120 μm, a deviation not easily detected visually in a real part.

A sensitivity analysis (similar to that outlined in Reference [28]) revealed that the most important source of the predicted arm warpage was tool/part interaction. As mentioned, perfect tool/part bonding was simulated in this case by setting the modulus of the interface shear layer equal to that of the aluminum tool. It was found that varying the assumed shear layer modulus had a tremendous impact on predicted warpage, causing a change in maximum warpage magnitude of the [90/+45/-45/0]<sub>6</sub> laminate of greater than a factor of 6, with lesser, but still signifi-

**Table 3. Experimental and predicted spring-back angles for angle laminates.**

Laminate Layup	Experimental Measurements	Model Prediction	Strain Non-Uniformity (Approximate)
[90] <sub>24</sub>	1.22°	0.05°	0.00°
[0] <sub>24</sub>	1.77°	1.79°	0.5°
[90/45/-45/0] <sub>6</sub>	1.92°	2.33°	0.7°

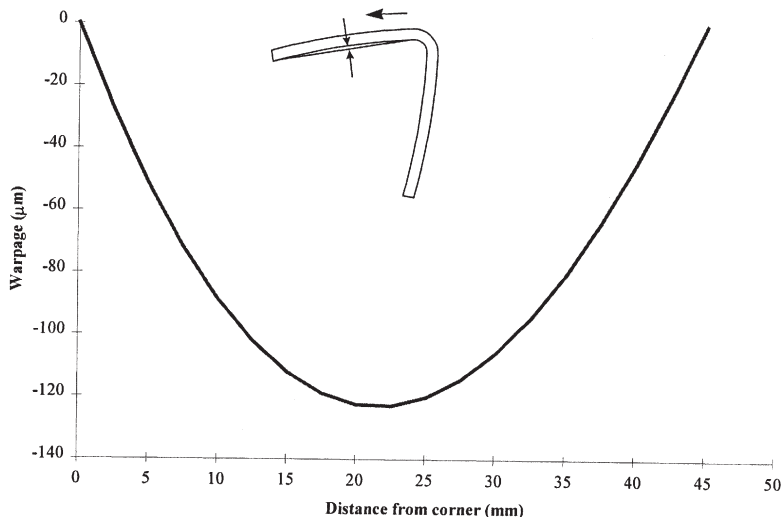


**Figure 12.** Predicted warpage of angle arms,  $[90/+45/-45/0]_6$  laminate assuming perfect tool/part bonding during processing.

cant effects on the warpage of the other symmetric laminates. As illustrated in Figure 13, shear layer modulus had a similar impact on predicted spring-back angle, resulting in values ranging from  $0.57^\circ$  to  $2.33^\circ$  for the  $[90/+45/-45/0]_6$  laminate.

The significance of the predicted effect of arm warpage on spring-back angle prompted re-examination of the experimental specimens. Careful measurements revealed that, although not noticed originally, the experimental specimens were indeed warped. As shown in Figure 14, the  $[90/+45/-45/0]_6$  laminates exhibited a maximum warpage of about  $20 \mu\text{m}$ . As also shown in this figure, both the shape and magnitude of the measured warpage could be closely matched by the model by employing a shear layer modulus of  $G_{SL} = 6 \text{ MPa}$ . Returning to Figure 13, however, it can be seen that using this shear layer modulus also gives much lower predictions for spring-back angle for both the  $[90/+45/-45/0]_6$  and the  $[0]_{24}$  laminates. Thus, in this case, the model was not able to predict well both warpage and spring-back angle at the same time, given the current assumptions made for materials properties and behaviour, especially with regard to the shear layer.

The unsymmetric laminate ( $[90_{12}/0_{12}]$ ) provides a final point of comparison between model predictions and experimental results. As shown in Figure 15, model predictions of arm warpage match the experimental measurements very well, both in terms of shape and absolute magnitude. A sensitivity analysis showed that in this case model predictions were not greatly influenced by the assumed shear layer modulus. Warpage in this case was not primarily related to tool part interaction, but rather to the very different strains on the top and bottom halves of the laminate.

To achieve improved predictions, to develop further confidence in the model,

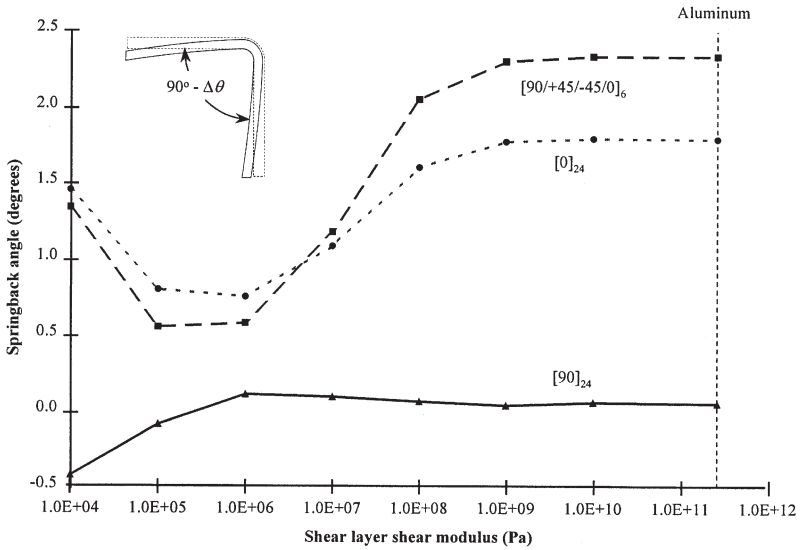


Figure 13. Effect of shear layer modulus on predicted laminate spring-back angle for symmetric laminates.

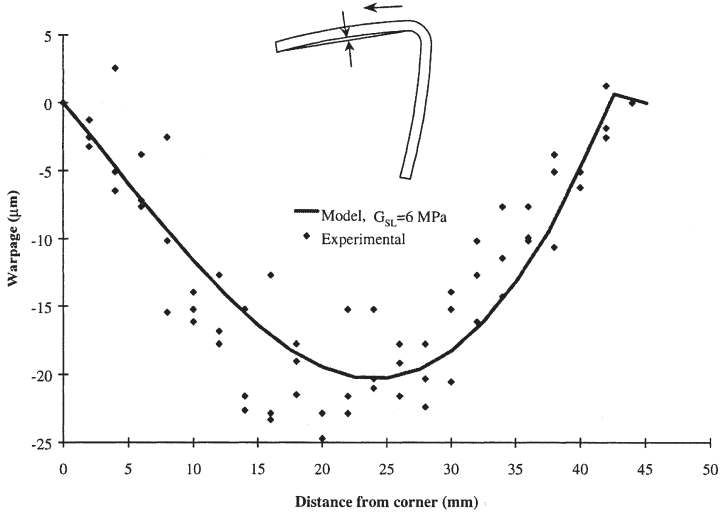
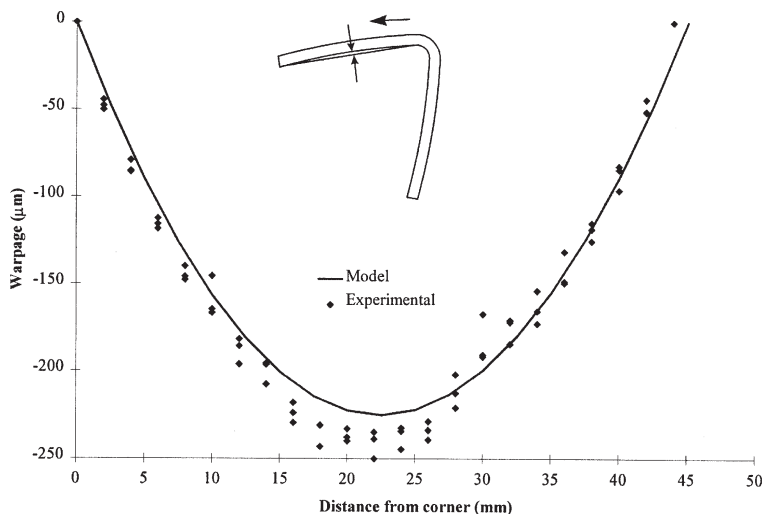


Figure 14. Comparison of measured arm warpage with model predictions for the [90/+45/-45/0]<sub>6</sub> laminate using a shear layer shear modulus of G<sub>SL</sub> = 6 MPa.



**Figure 15.** Comparison of measured arm warpage with model predictions for the  $[90_{12}/0_{12}]$  laminate. Note that warpage is not significantly affected by shear layer modulus for this case.

and to improve the model, there is a need for a body of case-studies, and characterisation of the materials and other parameters required by the model. This is an iterative process, as many of the parameters required by the model have never been of interest previously in demand before. However, there is an increasing body of case-studies to consider (e.g. References [28,31,32]), which overall show that, while requiring further refinement, the model described in this paper provides a good base for the prediction of residual stresses and deformations in composite structures of industrial interest.

## SUMMARY AND CONCLUSIONS

An integrated model for prediction of process-induced deformation during the processing of composite structures has been developed. A plane strain finite element model employing an incremental, instantaneously linear elastic, plane strain formulation is used to analyse all five major sources of process-induced deformation identified from the literature including: thermal strains, resin cure shrinkage strains, gradients in temperature and resin degree of cure, resin flow, and mechanical constraints caused by tooling. The integration of the analyses for all of these sources allows the model to be employed as a research tool to identify and focus effort on major process drivers and their variability.

The combination of an optimised solution strategy and advances in desktop computing capabilities allows rapid analysis of composite structures of intermedi-

ate size and complexity using very modest computational resources. The developed model can therefore also be a useful tool for the composite processor, assisting in tool and structure design, and in the development of robust, optimised autoclave process cycles.

A representative case study is presented, comparing model spring-back and warpage predictions with experimental measurements for a series of simple L-shaped laminates. This study shows that, for symmetric laminates, the model can predict both trends in spring-back angle with laminate layup and the warped shape of the laminate. Also, the model is capable of predicting both warpage shape and magnitude for the single type of unsymmetric laminate examined. However, for the symmetric laminates, both warpage and spring-back magnitudes cannot be successfully predicted simultaneously using the assumptions that have been made. The most likely source of this discrepancy is believed to be an overly simplified model for tool/part interaction (i.e. the elastic shear layer). The reader is referred to more case studies that provide further evidence of the applicability of the model [e.g. References 28, 32].

Not surprisingly, a number of topics require further investigation. There can never be enough experimental/numerical case studies to determine the relative contributions and the interactions of various stress and deformation mechanisms in different types of structures. A much better understanding is required, for example, of tool/part interaction, both in terms of how it may be characterised and modelled. Although tool constraints are known by industry to influence part warpage [29,30], only recently has effort been expended to examine this phenomenon scientifically [32]. Improved techniques are also required for characterisation of material property development during processing as well as measurement of stress and deformation development throughout processing.

## NOMENCLATURE

- $a_{Tg}$  = resin glass transition temperature development model constant
- $\underline{\mathbf{B}}$  = shape function derivative matrix
- $\mathbf{[C]}$  = ply plane strain stiffness matrix ( $3 \times 3$ ) in element local axes
- $\mathbf{[C]}$  = ply stiffness matrix
- $E_{ii}$  = elastic moduli
- $E_r$  = resin elastic modulus (isotropic)
- $E_r^0$  = resin modulus development model constant
- $E_r^\infty$  = resin modulus development model constant
- $\{\mathbf{F}\}$  = global nodal load vector
- $\{\mathbf{f}\}_e$  = element nodal load vector
- $\{\mathbf{f}_i\}_e$  = contribution of element initial strains to the element nodal load vector
- $\{\mathbf{F}_B\}$  = global body force vector
- $\{\mathbf{F}_{TR}\}$  = tool removal global nodal load vector

- $\{\mathbf{f}_\sigma\}_e$  = element nodal constraint load vector  
 $G_{ij}$  = shear moduli  
 $G_{SL}$  = shear layer shear modulus  
 $[\mathbf{J}]$  = Jacobian Matrix  
 $k$  = effective plane strain bulk modulus  
 $[\mathbf{k}]_e$  = element stiffness matrix  
 $[\mathbf{K}]$  = global stiffness matrix  
 $[\mathbf{K}_{TR}]$  = tool removal simulation global stiffness matrix  
 $[\mathbf{N}]$  = element shape function matrix  
 $[\mathbf{S}^*]$  = ply 3-D compliance matrix ( $6 \times 6$ ) in ply local axes  
 $[\mathbf{S}'_e]$  = ply 3-D compliance matrix ( $6 \times 6$ ) in element local axes  
 $[\mathbf{S}]$  = ply plane strain compliance matrix ( $3 \times 3$ ) in element local axes  
 $t$  = time  
 $T$  = temperature  
 $T_0$  = initial temperature or reference temperature  
 $T^*$  = difference between resin temperature and its instantaneous  $T_g$   
 $T_{C1}^*$  = resin modulus development model constant  
 $T_{C2}^*$  = resin modulus development model constant  
 $T_g$  = glass transition temperature  
 $T_g^0$  = uncured resin glass transition temperature  
 $[\mathbf{T}_\beta]$  = stress/strain transformation matrix (ply local axes to element local axes)  
 $[\mathbf{T}_\theta]$  = stress/strain transformation matrix (element local axes to global axes)  
 $V_f$  = fibre volume fraction  
 $\alpha$  = resin degree of cure  
 $\alpha_{ic}^S$  = composite material cure shrinkage coefficients in material principal directions  
 $\alpha_{ic}^T$  = composite coefficients of thermal expansion in material principal directions  
 $\beta$  = angle between element local and global coordinate systems  
 $\Delta t$  = time step  
 $\Delta\theta$  = spring-back angle (positive spring-back defined as a *reduction* in included angle)  
 $\{\delta\}_e$  = element nodal displacement vector  
 $\{\delta\}$  = global nodal displacement vector  
 $\{\delta_{TR}\}$  = global tool removal nodal displacement vector  
 $\{\epsilon\}_e$  = element strain vector  
 $\{\epsilon_0\}$  = ply initial strain vector ( $3 \times 1$ ) in global axes  
 $\{\epsilon_0^*\}$  = ply 3-D initial strain vector ( $6 \times 1$ ) in ply local axes  
 $\{\epsilon_0'\}$  = ply 3-D initial strain vector ( $6 \times 1$ ) in element local axes  
 $\{\bar{\epsilon}_0\}$  = ply plane strain initial strain vector ( $3 \times 1$ ) in element local axes  
 $\{\epsilon_\sigma\}_e$  = element constraint strain vector

- $\{\Phi\}$  = global surface traction vector
- $\Gamma$  = boundary surface area
- $\nu_{ij}$  = Poisson's ratios
- $\Omega$  = domain volume
- $\theta$  = ply orientation angle
- $\theta_i$  = "included" angle for a curved shape

## ACKNOWLEDGEMENTS

This work was supported by funding from the Natural Sciences and Engineering Research Council of Canada. We would also like to gratefully acknowledge the significant interaction and support from our colleagues at The University of British Columbia and The Boeing Company, particularly Pascal Hubert, Göran Fernlund, Robert Courdji, Larry Ilcewicz, Kurtis Willden, Karl Nelson, Bill Avery and Gerry Mabson.

## APPENDIX A

### Equations and Algorithms

#### *CALCULATION OF INITIAL STRAIN VECTOR $\{\epsilon_0\}$*

The nodal forces arising from the change in thermal and cure shrinkage strains (denoted as the "initial strains") during each solution time step are the only contributors to the global load vector in the current model. Calculation of the initial strain vector for each ply arising from the change in these thermal and cure shrinkage strains during a time step,  $\{\epsilon_0\}$  is performed as follows.

First, determine the change in ply thermal and cure shrinkage strains in the ply principal directions  $i$ . Thermal strains are calculated as

$$\epsilon_i^T = \alpha_{ic}^T (T^k - T^{k-1}) \quad (22)$$

where  $\alpha_{ic}^T$  are the material thermal expansion coefficients (computed from micromechanics models) and  $T^k$  and  $T^{k-1}$  are the average element temperatures at the start and end of the time step, respectively. Cure shrinkage strains are calculated similarly as

$$\epsilon_i^S = \alpha_{ic}^S (\epsilon_r^{S(k)} - \epsilon_r^{S(k-1)}) \quad (23)$$

where  $\alpha_{ic}^S$  are the composite cure shrinkage coefficients (again calculated from micromechanics models) and  $\epsilon_r^{S(k)}$  and  $\epsilon_r^{S(k-1)}$  are respectively the total resin *linear* cure shrinkage strains at the start and end of the time step.

We then define a 3-D initial strain vector,  $\{\epsilon_0^*\}$ , where:

$$\{\epsilon_0^*\} = \{\epsilon_{0(1)} \ \epsilon_{0(2)} \ 0 \ \epsilon_{0(3)} \ 0 \ 0\}^T \tag{24}$$

and  $\epsilon_{0(i)}$  is the initial strain in the direction  $i$ , equal to the sum of the thermal expansion and cure shrinkage strains in that direction. This vector is then transformed to the element local axes using:

$$\{\epsilon'_0\} = [\mathbf{T}_\theta]^{-1} \{\epsilon_0^*\} \tag{25}$$

where  $[\mathbf{T}_\theta]$  is the stress/strain transformation matrix defined in Equation (9) with the ply angle  $\theta$  defined in Figure 2(a).

Imposing the plane strain condition by suppressing all out-of-plane strains, we define a *plane strain initial strain* vector in the element local axes,  $\{\bar{\epsilon}_0\}$ , where:

$$\{\bar{\epsilon}_0\}^T = \{\bar{\epsilon}_{0(x')} \ \bar{\epsilon}_{0(z')} \ \bar{\gamma}_{0(x'z')}\} \tag{26}$$

This vector can be calculated by forcing all out-of-plane strains to zero and determining the resulting change in in-plane strains, using the fact that change in in-plane loads during this procedure will be identically zero. It can be shown that the resulting plane strain initial strain vector will then be:

$$\{\bar{\epsilon}_0\} = \{\epsilon'_{0(1)}\} + [\mathbf{C}'_1]^{-1} [\mathbf{C}'_2] \{\epsilon'_{0(2)}\} \tag{27}$$

where  $\{\epsilon'_{0(1)}\}$  and  $\{\epsilon'_{0(2)}\}$  are respectively the in-plane and out-of-plane terms of the transformed 3-D initial strain vector, i.e.,

$$\{\epsilon'_{0(1)}\} = \{\epsilon'_{0(x')} \ \epsilon'_{0(z')} \ \gamma'_{0(x'z')}\}; \ \{\epsilon'_{0(2)}\} = \{\epsilon'_{0(y')} \ \gamma'_{0(x'y')} \ \gamma'_{0(y'z')}\} \tag{28}$$

and  $[\mathbf{C}'_1]$  and  $[\mathbf{C}'_2]$  are:

$$[\mathbf{C}'_1] = \begin{bmatrix} C'_{11} & C'_{14} & 0 \\ C'_{14} & C'_{44} & 0 \\ 0 & 0 & C'_{55} \end{bmatrix}; \ [\mathbf{C}'_2] = \begin{bmatrix} C'_{12} & C'_{13} & 0 \\ C'_{24} & C'_{34} & 0 \\ 0 & 0 & C'_{66} \end{bmatrix} \tag{29}$$

where  $C'_{ij}$  are the terms of the *transformed 3-D stiffness matrix* defined by  $[\mathbf{C}'] = [\mathbf{S}']^{-1}$  where  $[\mathbf{S}']$  is defined in Equation (8).

In the final step of this procedure, the ply internal strain vector in the global axes is calculated using:

$$\{\epsilon_0\} = [\mathbf{T}_\beta]^{-1}\{\bar{\epsilon}_0\} \tag{30}$$

where  $[\mathbf{T}_\beta]$  transformation matrix defined in Equation (14) with  $\beta$  defined in Figure 2(b).

*CALCULATION OF ELEMENT CONSTRAINT STRAIN VECTOR  $\{\epsilon_\sigma\}_e$*

We define an element strain and an element “constraint”<sup>2</sup> strain  $\{\epsilon_\sigma\}_e$ . Element constraint strain is defined as the difference between element thermal and cure shrinkage strains and the *total* element strain,  $\{\epsilon\}_e$ , i.e.,

$$\{\epsilon_\sigma\}_e = \{\epsilon\}_e - \{\epsilon_0\}_e \tag{31}$$

To solve for the change in element constraint strain vector during a calculation time step, we first determine the change in the *element* initial strain vector,  $\{\Delta\epsilon_0\}_e$ , from the initial strain vectors of all the plies contained in that element. The first step in this calculation is determination of the change in element initial load vector caused by the initial strains of all plies within that element using:

$$\{\Delta\mathbf{f}_0\}_e = \int_{\Omega_e} [\mathbf{B}]^T [\mathbf{C}] \{\Delta\epsilon_0\} d\Omega \tag{32}$$

where both the stiffness matrix  $[\mathbf{C}]$  and the initial strain vector  $\{\Delta\epsilon_0\}$  vary from ply to ply. After calculation of the element stiffness matrix,  $[\mathbf{k}]_e$ , we then solve for the change in element nodal displacements that would be generated from the change in initial strains using

$$\{\Delta\delta_0\}_e = [\mathbf{k}]_e^{-1} \{\Delta\mathbf{f}_0\}_e \tag{33}$$

applying to the element the minimum number of constraints required to prevent free-body rotation as shown in Figure 16(a).

From the calculated change in element nodal displacements,  $\{\Delta\delta_0\}_e$ , we then calculate the change in the element initial strain vector,  $\{\Delta\epsilon_0\}_e$ . Finally, as illustrated in Figure 16(b), after solving for the change in global displacements during the step, the *total* change in strains for each element,  $\{\Delta\epsilon\}_e$ , are determined and the constraint strain vector for each element calculated using Equation (31) above.

The algorithm used to calculate element constraint strain is as follows:

1. **Calculate** element stiffness matrix,  $[\mathbf{k}]_e$ , and change in initial load vector  $\{\Delta\mathbf{f}_0\}_e$ .

---

<sup>2</sup>These strains are those which, because of geometrical constraints, lead to stress development. We have deliberately refrained from using the term “mechanical” strains to avoid confusion with strains arising from mechanical loads.

2. **Apply** element essential boundary conditions.
3. **Calculate** change in element nodal displacements and element strains due to internal strains,  $\{\Delta\delta_0\}_e$  and  $\{\Delta\varepsilon_0\}_e$  respectively.
4. **Solve** for change in global nodal displacements during the step,  $\{\Delta\delta\} = [\mathbf{K}]^{-1}\{\mathbf{F}\}$ .
5. **Calculate** actual change in element strains  $\{\Delta\varepsilon\}_e$  during the step.
6. **Calculate** change in element constraint strains during step,  $\{\Delta\varepsilon_\sigma\}_e = \{\Delta\varepsilon\}_e - \{\Delta\varepsilon_0\}_e$ .
7. **Add contribution** of change in element constraint strain during step to total constraint strain.

**CALCULATION OF ELEMENT CONSTRAINT LOAD VECTOR  $\{f_\sigma\}_e$**

In order to perform the tool removal simulation, the constraining loads applied to the nodes of each element by its neighbours must be calculated. Since material mechanical properties change during processing, this calculation must be performed at each time step and the results summed to arrive at the element constraint loads at any given time, i.e.,

$$\{f_\sigma\}_{ek} = \sum_{n=1}^k \{\Delta f_\sigma\}_{en} \tag{34}$$

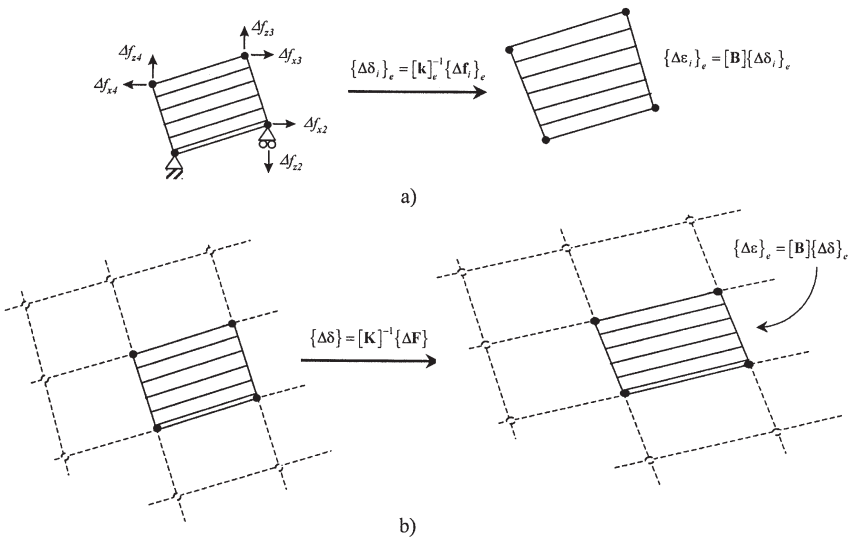


**Figure 16.** Calculation of changes in element strain vectors during a time step: (a) initial strain vector (arising from initial ply strain) and (b) total strain vector (arising from all sources, including initial strains).

where  $k$  is the time step number. The value of  $\{\Delta \mathbf{f}_\sigma\}_e$  is determined from the change in element constraint strains in the step by replacing the *ply* initial strain vector,  $\{\Delta \epsilon_0\}$  in Equation (32) with the *element* constraint strain vector,  $\{\Delta \epsilon_\sigma\}_e$ , i.e.,

$$\{\Delta \mathbf{f}_\sigma\}_e = \int_{\Omega_e} [\mathbf{B}]^T [\mathbf{C}] \{\Delta \epsilon_\sigma\}_e d\Omega \tag{35}$$

Note that in this case while the stiffness matrix  $[\mathbf{C}]$  again varies from ply to ply,  $\{\Delta \epsilon_\sigma\}_e$  is the same for all plies in the element.

The algorithm used to determine the element constraint load vector,  $\{\mathbf{f}_\sigma\}_e$ , is as follows:

1. **Calculate** the ply compliance matrix  $[\mathbf{S}^*]$  in ply local axes [see Equation (7)].
2. **Loop** over all plies in the element.
3. **Transform**  $[\mathbf{S}^*]$  to element local axes to obtain  $[\underline{\mathbf{S}}']$  [see Equation (8)].
4. **Calculate** material plane strain stiffness matrix  $[\underline{\mathbf{C}}]$  [see Equation (12)].
5. **Transform**  $[\underline{\mathbf{C}}]$  to global axes to obtain  $[\mathbf{C}]$  [see Equation (13)].
6. **Calculate**  $\{\Delta \mathbf{f}_\sigma\}_e$  for the ply.
7. **Add contribution** of ply load,  $\{\Delta \mathbf{f}_\sigma\}_e$ , to element load,  $\{\mathbf{f}_\sigma\}_e$ .

**PLY MICROMECHANICS MODEL**

Given as inputs the transversely isotropic mechanical properties of the fibres ( $E_{11f}$ ,  $E_{33f}$ ,  $G_{13f}$ ,  $\nu_{13f}$ , and  $\nu_{23f}$ ), the properties of the isotropic resin ( $E_r$ ,  $\nu_r$ ) and the fibre volume fraction,  $V_f$ , ply mechanical properties are calculated as follows using a micromechanics model from Bogetti and Gillespie [11]:

*In-Plane Moduli:*

$$E_{11} = E_{11f}V_f + E_r(1 - V_f) + \left[ \frac{4(\nu_r - \nu_{13f}^2)k_f k_r G_r (1 - V_f)V_f}{(k_f + G_r)k_r + (k_f - k_r)G_r V_f} \right] \tag{36}$$

where

$$G_r = \frac{E_r}{2(1 + \nu_r)} \tag{37}$$

$$E_{22} = E_{33} = \frac{1}{(1/4k_T) + (1/4G_{23}) + (\nu_{12}^2 / E_{11})} \tag{38}$$

*Shear Moduli:*

$$G_{12} = G_{13} = G_r \left[ \frac{(G_{13f} + G_r) + (G_{13f} - G_r)V_f}{(G_{13f} + G_r) - (G_{13f} - G_r)V_f} \right] \tag{39}$$

$$G_{23} = \frac{G_r [k_r (G_R + G_{23f}) + 2G_{23f}G_r + k_r (G_{23f} - G_r)V_f]}{k_r (G_{23f} + G_r) + 2G_{23f}G_r - (k_r + 2G_r)(G_{23f} - G_r)V_f} \quad (40)$$

where

$$G_{23f} = \frac{E_{33f}}{2(1 + \nu_{23f})} \quad (41)$$

Poisson's ratios

$$\nu_{12} = \nu_{13} = \nu_{13f}V_f + \nu_r(1 - V_f) + \left[ \frac{(\nu_r - \nu_{13f})(k_r - k_f)G_r(1 - V_f)V_f}{(k_f + G_r)k_r + (k_f - k_r)G_rV_f} \right] \quad (42)$$

$$\nu_{23} = \frac{2E_{11}k_T - E_{11}E_{22} - 4\nu_{13}^2k_T E_{22}}{2E_{11}k_T} \quad (43)$$

In the above,  $k$  is the so-called “isotropic plane strain bulk modulus” [11] defined by

$$k = \frac{E}{2(1 - \nu - 2\nu^2)} \quad (44)$$

and  $k_T$  is the effective plane strain bulk modulus of the composite defined by

$$k_T = \frac{(k_f + G_r)k_r + (k_f - k_r)G_rV_f}{(k_f + G_r) - (k_f - k_r)V_f} \quad (45)$$

*Calculation of Thermal and Cure Shrinkage Strains*

Ply strains in the material principal directions arising from strains of the constituent resin and fibre are calculated from the fibre and resin mechanical properties and strains as follows:

$$\epsilon_1 = \frac{\epsilon_{1f}E_{11f}V_f + \epsilon_r E_r(1 - V_f)}{E_{11f}V_f + E_r(1 - V_f)} \quad (46)$$

$$\epsilon_2 = \epsilon_3 = (\epsilon_{2f} + \nu_{13f}\epsilon_{1f})V_f + (\epsilon_r + \nu_r\epsilon_r)(1 - V_f)$$

$$-[\nu_{13f}V_f + \nu_r(1 - V_f)] \left[ \frac{\epsilon_{1f}E_{1f}V_f + \epsilon_R E_r(1 - V_f)}{E_1V_f + E_r(1 - V_f)} \right] \quad (47)$$

To calculate composite thermal expansion coefficients ( $a_{ic}^T$ ), the resin and fibre strains are replaced by their respective thermal expansion coefficients.

## REFERENCES

1. Hubert, P. and Poursartip, A., "A Review of Flow and Compaction Modelling Relevant to Thermoset Matrix Laminate Processing," *Journal of Reinforced Plastics and Composites*, 17(4):286–318 (1998).
2. Mijovic, J. and Wijaya, J., "Effects of Graphite Fiber and Epoxy Matrix Physical Properties on the Temperature Profile Inside Their Composite during Cure," *SAMPE Journal* 25(2):35–39 (1989).
3. Bogetti, T.A. and Gillespie Jr. J.W., "Two-Dimensional Cure Simulation of Thick Thermosetting Composites," *Journal of Composite Materials*, 25(3):239–273 (1991).
4. Kenny, J.M., "Integration of Process Models with Control and Optimization of Polymer Composites Fabrication," *Proceedings of the Third Conference on Computer Aided Design in Composite Materials Technology*, Newark, DE, USA, pp. 530–544 (1992).
5. Davé, R., Kardos, J.L. and Dudukovic, M.P., "A Model for Resin Flow during Composite Processing: Part 1—General Mathematical Development," *Polymer Composites*, 8(1):29–38 (1987).
6. Hubert, P., Vaziri, R., and Poursartip, A., "A Two Dimensional Flow Model for the Process Simulation of Complex Shape Composite Laminates", *International Journal for Numerical Methods in Engineering*, 44(1):1–26 (1999).
7. Hahn, H.T. and Pagano, N.J., "Curing Stresses in Composite Laminates," *Journal of Composite Materials*, 9, pp. 91–108 (1975).
8. White, S.R. and Hahn, H.T., "Process Modeling of Composite Materials: Residual Stress Development during Cure. Part I. Model Formulation," *Journal of Composite Materials*, 26(16):2402–2422 (1992).
9. Loos, A.C. and Springer, G.S., "Curing of Epoxy Matrix Composites," *Journal of Composite Materials*, 17(2):135–169 (1983).
10. Mallow, A.R., Muncaster, F.R., and Campbell, F.C., "Science Based Cure Model for Composites," *Proceedings of the American Society for Composites, First Technical Conference*, Dayton, OH, USA, pp. 171–186 (1986).
11. Bogetti, T.A. and Gillespie Jr., J.W., "Process-Induced Stress and Deformation in Thick-Section Thermoset Composite Laminates", *Journal of Composite Materials*, 26(5):626–660 (1992).
12. Hubert, P., Johnston, A., Vaziri, R., and Poursartip, A., "A Two-Dimensional Finite Element Processing Model for FRP Composite Components", *Proceedings of The 10th International Conference on Composite Materials (ICCM-10)*, Whistler, B.C., Canada, III-149–III-156 (1995).
13. Hahn, H.T., "Effects of Residual Stresses in Polymer Matrix Composites," *Journal of the Astronautical Sciences*, 32(3):253–267 (1984).
14. Adolf, D., and Martin, J.E., "Calculation of Stresses in Crosslinking Polymers," *Journal of Composite Materials*, 30(1):13–34 (1996).
15. Radford, D.W., "Cure Shrinkage Induced Warpage in Flat Uni-Axial Composites," *Journal of Composites Technology and Research*, 15(4):290–296 (1994).
16. Nelson, R.H. and Cairns, D.S., "Prediction of Dimensional Changes in Composite Laminates during Cure," *34th International SAMPE Symposium*, May 8–11, pp. 2397–2410 (1989).
17. Shi, J. and Flannagan, R., "A Simple Spring-Damper-Slider Model for Laminate Slippage," *Proceedings of The 10th International Conference on Composite Materials (ICCM - 10)*, A. Poursartip and K. Street, Eds., Whistler, B.C., Canada, August, III-197–III-204 (1995).
18. COMPRO, Finite Element Software, © The University of British Columbia.
19. Bogetti, T.A., "Process-Induced Stress and Deformation in Thick-Section Thermosetting Composites" *Technical Report CCM-89-32*, Center for Composite Materials, University of Delaware, Newark, Delaware (1989).
20. Li, M.C., Wu, J.J., Loos, A.C., and Morton, J., "A Plane-Strain Finite Element Model for Pro-

- cess-Induced Residual Stresses in a Graphite/PEEK Composite,” *Journal of Composite Materials*, 31(3)212–243 (1997).
21. Cook, R.D., Malkus, D.S. and Plesha, M.E., *Concepts and Applications of Finite Element Analysis*, Third Edition, John Wiley & Sons, New York (1989).
  22. Felippa, C.A., “Solution of Linear Equations with Skyline-Stored Symmetric Matrix,” *Computers and Structures* 5(1):13–29 (1975).
  23. Fahmy, A.A. and Ragai-Ellozy, A.N., “Thermal Expansion of Laminated Fiber Composites in the Thickness Direction,” *Journal of Composite Materials* 8, pp. 90–92 (1974).
  24. Stephan, A., Schwinge, E., Müller, J., and Öry, H., “On the Springback Effect of CFRP Stringers: An Experimental, Analytical and Numerical Analysis”, *28th International SAMPE Technical Conference*, November 4–7, pp. 245–254 (1996).
  25. Johnston, A., *An Integrated Model of the Development of Process-Induced Deformation in Autoclave Processing of Composites Structures*, Ph.D. thesis, The University of British Columbia, Vancouver (1997).
  26. Rennick, T.S. and Radford, D.W., “Components of Manufacturing Distortion in Carbon Fiber/Epoxy Angle Brackets”, *28th International SAMPE Technical Conference*, November 4–7, 189–197 (1996).
  27. Patterson, J.M., Springer, G.S., and Kollár, L.P., “Experimental Observations of the Spring-back phenomena”, *Eighth International Conference on Composite Materials (ICCM-VIII)*, 10-D-1–10-D-8 (1991).
  28. Johnston, A., Hubert, P., Nelson, K., and Poursartip, A., “A Sensitivity Analysis of Factors Affecting the Warpage of a Composite Structure”, *43rd International SAMPE Symposium and Exhibition*, Anaheim, CA, USA, May 31–June 4 (1998).
  29. Borstell, H. and Turner, K.J., “Tooling for Autoclave Molding,” *Engineered Materials Handbook, Vol. 1: Composites*, Dostal, C.A., Woods, M.S., and Ponke, A.W., Eds., ASM International, Metals Park, Ohio, USA, pp. 578–589 (1987).
  30. Pagliuso, S., “Warpage, a Nightmare for Composite Parts Producers,” *Proceedings of The 4th International Conference on Composite Materials (ICCM-4)*, T. Hayashi, K. Kawata, and S. Umekawa, Eds., Tokyo, Japan, pp. 1617–1623 (1982).
  31. Fernlund, G., Poursartip, A., Russell, J., Nelson, K., Wilenski M., and Swanstrom, F., “Process Modeling for Dimensional Control—Sensitivity Analysis of a Composite Spar Process”, *Proceedings of 44th International SAMPE Symposium and Exhibition*, Long Beach, California, May 23–27 (1999).
  32. Fernlund, G. and Poursartip, A., “The Effect of Tooling Material, Cure Cycle, and Tool Surface Finish on Spring-in of Autoclave Processed Curved Composite Parts” *Proceedings of ICCM-12*, paper 690, ISBN 2-9514526-2-4, Paris, France, July 5-9 (1999).